Available online at www.sciencedirect.com
SCIENCE DIRECT®
PERGAMON
International Journal of Heat and Mass Transfer 46 (2003) 2051–2063
International Journal of HEAT and MASS TRANSFER
www.elsevier.com/locate/ijhmt

Analytical and experimental investigation on the operational characteristics and the thermal optimization of a miniature heat pipe with a grooved wick structure

Sung Jin Kim *, Joung Ki Seo, Kyu Hyung Do

Department of Mechanical Engineering, Korea Advanced Institute of Science and Technology, Taejon 305-701, South Korea

Received 21 June 2002; received in revised form 11 October 2002

Abstract

A mathematical model for heat and mass transfer in a miniature heat pipe with a grooved wick structure is developed and solved analytically to yield the maximum heat transport rate and the overall thermal resistance under steady-state conditions. The effects of the liquid–vapor interfacial shear stress, the contact angle, and the amount of initial liquid charge have been considered in the proposed model. In particular, a novel method called a modified Shah method is suggested and validated; this method is an essential feature of the proposed model and accounts for the effect of the liquid–vapor interfacial shear stress. In order to verify the model, experiments for measuring the maximum heat transport rate and the overall thermal resistance are conducted. The analytical results for the maximum heat transport rate and the total thermal resistance based on the proposed model are shown to be in close agreement with the experimental results. From the proposed model, numerical optimization is performed to enhance the thermal performance of the miniature heat pipe. It is estimated that the maximum heat transport rate of outer diameter 3 and 4 mm heat pipes can be enhanced up to 48% and 73%, respectively, when the groove wick structure is optimized from the existing configurations. Similarly, the total thermal resistance of these heat pipes can be reduced by 7% and 11%, respectively, as a result of optimization.

1. Introduction

Miniature heat pipes with a small outer diameter (OD hereafter) of 3 or 4 mm have been widely used in cooling microprocessors in notebook and desktop PC applications due to their powerful heat transfer capability and small size. As the power density of critical electronic components is increased, the need for a heat pipe with a higher heat transport rate and a lower thermal resistance is greater than ever in the development of future electronic equipment. In order to cope with this practical demand, it is necessary to enhance the thermal performance of a miniature heat pipe, by optimizing the wick structure of a heat pipe.

Since Cotter [1] introduced the concept of a micro heat pipe, many investigations have been conducted to characterize the thermal performance of micro/miniature heat pipes used as a chip/module-level cooling device for electronic packaging. In the early stage of this research, Babin et al. [2] developed a simplified numerical model and conducted experiments for measuring the maximum heat transport rate of a micro heat pipe, which served as a foundation for subsequent research. Wu and Peterson [3] investigated the transient behavior of a micro heat pipe numerically and compared their numerical results for the maximum heat transport rate in steady-state operation with the experimental data of Babin et al. Khrustalev and Faghri [4] developed a numerical model for heat and mass transfer characteristics occurring in a micro heat pipe with triangular grooves. Their results showed that the liquid–vapor interfacial shear stress and the contact angle could significantly influence the maximum heat transport rate of micro heat

* Corresponding author. Tel.: +82-42-869-3043; fax: +82-42-869-8207.

0017-9310/03/$ - see front matter
doi:10.1016/S0017-9310(02)00504-5

Nomenclature

D	diameter
f	skin friction factor
h	heat transfer coefficient
h_b	container wall thickness in Fig. 2
h_{fg}	latent heat of vaporization
h_g	groove height in Figs. 1 and 2
h_m	meniscus height in Figs. 1 and 2
k	thermal conductivity
K	permeability of wick structure
L	length
N	total number of groove
P	pressure
Q	heat rate
r	radius
R	thermal resistance
R_g	ideal gas constant
Re_r	Reynolds number in radial direction
t_b	groove bottom width in Fig. 1(b)
t_s	groove land width in Fig. 1(b)
T	temperature
u	velocity
x	distance from beginning of the evaporator section

Greek symbols

β	tilt angle of heat pipe
ε	porosity of wick structure
γ	half angle of a groove ($= \pi/N$)
μ	viscosity
θ	solid–liquid contact angle
ρ	density
σ	surface tension coefficient
τ	shear stress
ξ	groove land angle in Fig. 1(b)
ζ	groove wall inclination angle in Fig. 1(b)

Subscripts

a	adiabatic section
b	liquid block
c	condenser section, capillary
crit	critical
D	Darcian
e	evaporator section
eff	effective
exp	experimental
h	hydraulic
i	liquid–vapor interface
ini	initial
l	liquid
p	pore
s	solid
v	vapor
w	wall
work	working

Superscript

–	average

pipes. Also, Khrustalev and Faghri [5] investigated the effect of the thin film evaporation at the evaporator section using a mathematical model developed for conventional and flat miniature axially grooved heat pipes. Hopkins et al. [6] conducted a numerical and experimental investigation on a flat plate heat pipe with a grooved wick structure, which is similar to the wick structure of the circular miniature heat pipe in the present study. Recently, Zhu and Vafai [7] developed a two-dimensional analytical model for low-temperature cylindrical heat pipes with a porous wick and obtained a closed-form solution based on the assumed velocity profiles of liquid and vapor. Oomi et al. [8] investigated the maximum heat transport rate of miniature heat pipes with a grooved wick structure using an experimental method disregarding the heat loss in the experimental apparatus.

If a mathematical model for predicting the thermal characteristics of a heat pipe with a specific wick structure were developed, it would be a useful tool for designing an optimized heat pipe with a higher thermal performance. Even though there already exists a numerical code developed by NASA to predict the maximum heat transport rate of a circular heat pipe with a grooved wick structure, it is not appropriate as an optimization tool because its numerical results do not agree well with the experimental results, as pointed out in [9]. The main objective of the present study is to develop a new mathematical model by which one can predict the thermal characteristics of the grooved wick heat pipe with reasonable accuracy. The proposed model includes the effects of the liquid–vapor interfacial shear stress, the contact angle, and the amount of initial liquid charge. In particular, a novel method called a modified Shah method is suggested to account for the effect of the liquid–vapor interfacial shear stress on the thermal performance of a heat pipe. In order to verify the proposed model, experiments for measuring the maximum heat transport rate and the thermal resistance are conducted and the experimental data are compared with the results obtained from the proposed model. Finally, the proposed model is applied to optimize the maximum

heat transport rate and the thermal resistance of the miniature heat pipe with a grooved wick structure, resulting in the enhancement of thermal performance.

2. Mathematical modeling

2.1. Model for the maximum heat transport capability

When a meniscus is formed at the liquid–vapor interface as shown in Fig. 1(b), the capillary pressure P_c can be calculated by the well-known Laplace–Young equation

$$P_c = P_v - P_l = \sigma\left(\frac{1}{r_{c1}} + \frac{1}{r_{c2}}\right), \tag{1}$$

where r_{c1} and r_{c2} are the principal capillary radii of the meniscus. Since r_{c2} is much larger than r_{c1}, it is quite reasonable to assume that $r_{c1} \approx r_c(x)$ and $r_{c2} \approx \infty$. The differential form of Eq. (1) then becomes

$$\frac{dP_v}{dx} - \frac{dP_l}{dx} = -\frac{\sigma}{r_c(x)^2}\frac{dr_c(x)}{dx}. \tag{2}$$

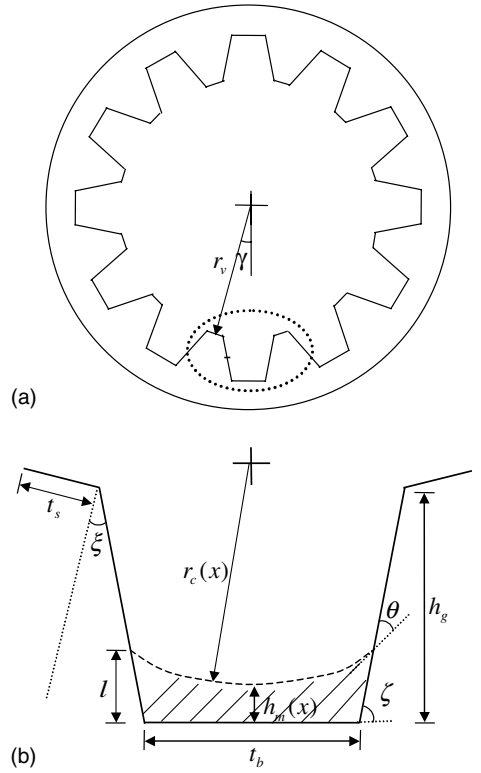

Fig. 1. Schematic diagram of the grooved wick structure: (a) cross-sectional view and (b) geometric shape and variables in a groove.

If we express the liquid and vapor pressure gradient terms in Eq. (2) using geometric variables and the capillary radius, Eq. (2) can be solved numerically.

By modeling the grooved wick structure in Fig. 1(a) as a porous medium, the liquid pressure gradient can be expressed by

$$\frac{dP_l}{dx} = -\frac{\mu_l u_D}{K}, \tag{3}$$

which is known as Darcy's law. Using the relationship between the Darcian velocity (u_D) and the averaged pore velocity (u_p), $u_D/u_p = \varepsilon$, and the mass flow rate in the wick structure, $\dot{m}_l = \rho_l A_p u_p N$, Eq. (3) becomes

$$\frac{dP_l}{dx} = -\frac{\mu_l \varepsilon u_p}{K} = -\frac{\mu_l \varepsilon \dot{m}_l}{\rho_l A_p N K}, \tag{4}$$

where the permeability of a groove with an arbitrary cross-section, K, can be written as [10]

$$K = \frac{D_{h,p}^2 \varepsilon}{2 f Re_{h,p}}. \tag{5}$$

For a closed circular flow passage, $fRe_{h,p}$ (called the Poiseuille number) equals 16, while for a flow passage with a different cross-section the Poiseuille number is different. However, the liquid flow passage of a heat pipe is not enclosed but open to the vapor core region where vapor flows in the direction opposite to the liquid flow. These counter-flows of liquid and vapor cause an additional shear stress at the liquid–vapor interface, which makes analysis of the liquid flow difficult. The effect of the counter-flows on the interfacial shear stress can be accounted for by introducing a correction factor, α, when substituting Eq. (5) into Eq. (4), which results in the following Eq. [11]:

$$\frac{dP_l}{dx} = -\frac{2\mu_l f Re_{h,p} \dot{m}_l}{\rho_l A_p N D_{h,p}^2}\alpha + \rho_l g \sin\beta, \tag{6}$$

where the last term is included for a pressure drop due to gravity. In Eq. (6), the Poiseuille number, $fRe_{h,p}$, the correction factor, α, the actual liquid flow area, A_p, and the mass flow rate of liquid, $\dot{m}_l$ need to be expressed in terms of the geometric variables and thermo-physical properties of the liquid in order to quantitatively evaluate the liquid pressure gradient.

Note that $fRe_{h,p}$ in Eq. (6) is the Poiseuille number for an open trapezoidal channel without liquid–vapor interfacial shear stress and α is the ratio of an actual liquid pressure gradient with the counter-flow effect included to an ideal liquid pressure gradient with zero vapor flow. This ratio can be expressed as

$$\alpha = 1 + F\psi, \tag{7}$$

where

$$\psi = \frac{D_{h,p}\tau_{v,i}}{\mu_l u_p} = \frac{D_{h,p} r_v}{2\mu_l u_p}\left(\frac{dP_v}{dx}\right),$$

F is a function of the geometric variables and the contact angle and ψ is the non-dimensional shear stress at the interface.

Quantitative evaluation of $fRe_{h,p}$ and α using the conventional CFD method is involved since the liquid flow passage is geometrically complex due to inclined walls and a curved interface. Moreover, the characteristics of counter-current flows make it even more complicated and require much effort and computational time. In order to overcome these difficulties, we suggest a powerful method called a modified Shah method, which is the essential feature of present model. Details are explained in Appendix A because it is rather involved mathematically. It is worth mentioning that the modified Shah method can be applied for an open channel with an arbitrary cross-section. Based on the modified Shah method, we suggest the correlations of $fRe_{h,p}$ and F at various contact angles for a trapezoidal open channel with a wall inclination angle ζ of 84° and 76° (for each OD 3 and 4 mm) in Table 1.

If we take into account the contact angle, which is an interfacial property of the solid–liquid pair (the grooved wall and the liquid), an actual liquid flow area below the meniscus, A_p, can be written for $r_c(x) \leqslant r_{c,crit}$ as

$$A_p = r_c(x)\cos(\theta+\xi-\gamma)\{2l + r_c(x)\sin(\theta+\xi-\gamma)\} - l^2\tan(\xi-\gamma) - r_c(x)^2\left\{\frac{\pi}{2} - (\theta+\xi-\gamma)\right\}, \quad (8)$$

where

$$l = \frac{2r_c(x)\cos(\theta+\xi-\gamma) - t_b}{2\tan(\xi-\gamma)},$$

$$r_{c,crit} = \frac{2h_g\tan(\xi-\gamma) + t_b}{2\cos(\theta+\xi-\gamma)}.$$

On the other hand, for $r_c(x) > r_{c,crit}$

$$A_p = h_g\{h_g\tan(\xi-\gamma) + t_b\} - \frac{1}{2}r_c(x)^2(\eta - \sin\eta), \quad (9)$$

where

$$\eta = 2\sin^{-1}\left\{\frac{2h_g\tan(\xi-\gamma) + t_b}{2r_c(x)}\right\}$$

and $r_{c,crit}$ is defined as a critical capillary radius beyond which the radius of curvature for the meniscus cannot increase without changing the given contact angle [6]. In other words, $r_c(x)$ becomes $r_{c,crit}$ when l in Eq. (8) equals h_g, as shown in Fig. 1(b).

The mass flow rate of liquid, $\dot{m}_l$, which is the final information required to determine the liquid pressure gradient, can be obtained from the energy balance at each section as

$$\dot{m}_l = -\dot{m}_v = -\frac{Q(x)}{h_{fg}}. \quad (10)$$

In the present study, it is assumed that a uniform heat flux is applied at the evaporator (condenser) section for heating (cooling). Note that the present model includes the effect of a liquid block [4] that is formed at the

Table 1
Correlations for Poiseuille number and F in Eq. (7)

Aspect ratio $(A_s)^a < 1.5$		Aspect ratio $\geqslant 1.5$	
$y_0 + a \times \exp(-b \times A_s) + c \times A_s$		$a \times \exp(-0.5 \times (\log(A_s/x_0)/b)^2)$	
Poiseuille number			
Groove wall inclination angle $(\zeta) = 84°$ (OD 3 mm heat pipe)			
y_0	$5.753\theta^{0.1841}$	a	$14.11\theta^{0.06009}$
a	$173.9 - 5.3737\theta + 0.0621\theta^2 - 0.0002\theta^3$	b	$2.083\theta^{0.0372}$
b	$8.899 - 0.1511\theta + 2.196\text{E}-3\theta^2 - 7.866\text{E}-6\theta^3$	x_0	$22.22\theta^{-0.3366}$
c	$2.172 + 0.0011\theta$		
Groove wall inclination angle $(\zeta) = 76°$ (OD 4 mm heat pipe)			
y_0	$6.391\theta^{0.1721}$	a	$11.23\theta^{0.09313}$
a	$137 - 5.008\theta + 0.07312\theta^2 - 0.0003808\theta^3$	b	$2.406\theta^{0.01303}$
b	$4.901 + 0.01448\theta$	x_0	$19.29\theta^{-0.3836}$
c	$-0.8141 + 0.141\theta - 2.762\text{E}-3\theta^2 - 1.758\text{E}-5\theta^3$		
Wall inclination angle $(\zeta) = 84°$ (OD 3 mm)		Wall inclination angle $(\zeta) = 76°$ (OD 4 mm)	
F in Eq. (7)			
$y_0 + a \times \exp(-b \times A_s)$			
y_0	$0.029 - 1.475\text{E}-4\theta + 1.331\text{E}-6\theta^2 + 3.059\text{E}-4\theta^3$	y_0	$0.057 - 5.749\text{E}-4\theta + 6.12\text{E}-6\theta^2$
a	$0.247 - 3.35\text{E}-3\theta + 2.396\text{E}-5\theta^2$	a	$0.250 - 4.87\text{E}-3\theta + 4.068\text{E}-5\theta^2$
b	$1.528 - 0.0168\theta + 1.417\text{E}-4\theta^2$	b	$2.054 - 0.04227\theta + 4.156\text{E}-4\theta^2$

[a] Aspect ratio is defined as (Wetted groove depth)/(Bottom groove width, t_b).

condenser section end cap due to a slight overcharging of the working fluid. Because the thermal conductivity of the liquid block is much lower than that of the solid wall, the liquid block acts as a thermal barrier for the condensation heat transfer. Accounting for the liquid block length, we can express heating and cooling conditions as follows:

$$Q(x)=\begin{cases}\frac{x}{L_e}Q_{in}, & 0\leqslant x\leqslant L_e\\ Q_{in}, & L_e\leqslant x\leqslant L_e+L_a\\ \left(1+\frac{L_e+L_a-x}{L_{eff,c}}\right)Q_{in}, & \\ \quad L_e+L_a\leqslant x\leqslant L_e+L_a+L_{eff,c}, & \end{cases} \tag{11}$$

where

$$L_{eff,c}=L_c-L_b.$$

The vapor pressure gradient appeared in Eq. (2), on the other hand, depends on the condition of heat loading because mass transfer associated with evaporation and condensation affects the vapor flow characteristics. For a two-dimensional incompressible vapor flow with evaporation and condensation at the liquid–vapor interface, Faghri [12] developed an analytical model for the vapor pressure distributions at each section using the continuity and momentum equations as

$$\frac{dP_v}{dx}=\begin{cases}2\left(-8|Re_e|-\frac{16}{3}Re_e^2\right)\left(\frac{\mu_v^2}{\rho_v r_v^4}\right)x, & \\ \quad 0\leqslant x\leqslant L_e, & \\ \left(\frac{-8\mu_v\bar{u}_{v,a}}{r_v^2}\right), & \\ \quad L_e\leqslant x\leqslant L_e+L_a & \\ 2\left(8|Re_c|-\frac{16}{3}Re_c^2\right)\left(\frac{\mu_v^2}{\rho_v r_v^4}\right)x+\left(\frac{16}{3}|Re_c|-8\right)\left(\frac{\mu_v\bar{u}_{v,a}}{r_v^2}\right), & \\ \quad L_e+L_a\leqslant x\leqslant L_e+L_a+L_{eff,c}, & \end{cases} \tag{12}$$

where

$$Re_{r,e}=\frac{Q_{in}}{2\pi L_e h_{fg}\mu_v},\quad Re_{r,c}=\frac{Q_{in}}{2\pi L_c h_{fg}\mu_v},\quad \bar{u}_{v,a}=\frac{Q_{in}}{\rho_v\pi r_v^2 h_{fg}}.$$

Assuming the vapor as an ideal gas, we can calculate $P_v(x)$ at $x=0$ using the ideal gas law.

Combining Eqs. (2), (6), and (12) yields an ordinary differential equation for $r_c(x)$ as

$$\frac{dr_c(x)}{dx}=\frac{r_c(x)^2}{\sigma}\left[\left(\frac{2\mu_l\dot{m}_l fRe_{h,p}}{\rho_l A_p N D_{h,p}^2}\alpha+\rho_l g\sin\beta\right)-\frac{dP_v}{dx}\right]. \tag{13}$$

Using Eqs. (7)–(12), the correlations of $fRe_{h,p}$ and F in Table 1, Eq. (13) can be cast into the following form of which the right-hand side is a function of several parameters:

$$\frac{dr_c(x)}{dx}=f(r_c(x),x,Q_{in},T_{work},\theta,\text{geometry},m_{ini},\beta). \tag{14}$$

Once all the variables are specified, Eq. (14) can be solved numerically using the fourth-order Runge–Kutta method. Note that all the thermo-physical properties are assumed to be constant and evaluated at the working temperature of the heat pipe.

In solving Eq. (14), an initial value of $r_c(x)$ at $x=0$ and a convergence criterion are necessary, and can be determined from physical insight. When a heat pipe transports heat in a steady-state, $r_c(x)$ and $h_m(x)$ in Fig. 1(b) increase non-linearly from the evaporator section to the condenser section. If a heat pipe is to transport a maximum amount of heat, a minimum capillary radius should be formed at the beginning of the evaporator section and a maximum capillary radius at the point where the liquid block starts in the condenser section [6]. In this situation, the minimum capillary radius can be evaluated from the groove geometry as in Eq. (15), which is used as the initial condition for $r_c(x)$ at $x=0$ for Eq. (14).

$$r_{c,min}=\frac{t_b}{2[\cos(\theta+\xi-\gamma)-\tan(\xi-\gamma)\{1-\sin(\theta+\xi-\gamma)\}]}. \tag{15}$$

Also, it is assumed that the maximum capillary radius equals the vapor core radius at $x=L_e+L_a+L_{c,eff}$ [4], which is regarded as the convergence criterion of the capillary radius for Eq. (15). The entire calculation procedure may be summarized as follows:

(1) Assume an initial value of $Q_{in}=0.1$ W in Eq. (14).
(2) Determine $r_{c,min}$ using Eq. (15).
(3) Calculate $r_c(x)$ using the fourth-order Runge–Kutta method.
(4) From 0 to x, calculate the total mass of the liquid in the grooves, m_l, and the vapor, m_v. Assume the remainder of the inner volume of the heat pipe is filled with the liquid m_{vir}.
(5) If the overall mass balance condition, $m_l+m_v+m_{vir}=m_{ini}$, is not satisfied, increase $x=x+\Delta x$ and return to step (3).
(6) If the overall mass balance condition holds but the convergence criterion fails ($r_c(x)<r_v$), increase $Q_{in}=Q_{in}+\Delta Q_{in}$ (typically, $\Delta Q_{in}=0.01$ W) and return to step (2). If both the mass balance condition and the convergence condition are satisfied at x, calculate the liquid block length using $L_b=(L_a+L_e+L_c)-x$ and regard Q_{in} as the maximum heat transport rate Q_{max} for the specified working temperature.

For numerical simulations, Δx is chosen to be $L_e/100$, which is shown through grid tests to be small enough not to affect the numerical results.

2.2. Model for the thermal resistance

The total thermal resistance is another important figure-of-merit of a heat pipe in addition to the maximum heat transport rate. To evaluate the total thermal resistance, a simplified model for the averaged thermal resistance of each section can be written as [13]

$$Q_{\text{in}} = \frac{T_{\text{w,e}} - T_{\text{v,e}}}{\overline{R}_{\text{e}}} = \frac{T_{\text{v,e}} - T_{\text{v,c}}}{\overline{R}_{\text{a}}} = \frac{T_{\text{v,c}} - T_{\text{w,c}}}{\overline{R}_{\text{c}}} = \frac{T_{\text{w,e}} - T_{\text{w,c}}}{\overline{R}_{\text{e}} + \overline{R}_{\text{a}} + \overline{R}_{\text{c}}} = \frac{\Delta T}{\overline{R}_{\text{tot}}}. \tag{16}$$

If we consider the vapor as an ideal gas, the vapor temperatures in the middle of the evaporator section and the condenser section can be related to the vapor pressures of each point by the Clausis–Clapeyron equation because the phase change occurs at these points. Because there is no heat transfer in a radial direction along the adiabatic section, we can express the relation among various temperature as

$$T_{\text{work}} \equiv T_{\text{v,a}} = T_{\text{w,a}} \cong \frac{T_{\text{v,e}} + T_{\text{v,c}}}{2}. \tag{17}$$

Because $P_{\text{v,e}}$ and $P_{\text{v,c}}$ are obtained in Section 2.1 and T_{work} is given, $\overline{R}_{\text{a}}$ can be derived using the Clausius–Clapeyron equation and Eq. (17) as

$$\overline{R}_{\text{a}} = \frac{T_{\text{v,e}} - T_{\text{v,c}}}{Q_{\text{in}}} = \frac{2}{CQ_{\text{in}}}\left(\sqrt{1 + (CT_{\text{work}})^2} - 1\right), \tag{18}$$

where

$$C = \frac{R_{\text{g}}}{h_{\text{fg}}} \ln\left(\frac{P_{\text{v,e}}}{P_{\text{v,c}}}\right).$$

In order to simplify the determination of the averaged thermal resistance of the evaporator section, $\overline{R}_{\text{e}}$, and the condenser section, $\overline{R}_{\text{c}}$ as shown in Fig. 2(a) and (b), the groove structure is approximated to be rectangular rather than trapezoidal because ζ is greater than 76° for all cases under consideration. Also, the temperature difference between the vapor and the liquid at the liquid–vapor interface is assumed to be small and negligible [1].

The local thermal resistance of the evaporator and condenser sections varies since the meniscus height, $h_{\text{m}}(x)$, changes along the axial direction. In this case, the averaged thermal resistance of the evaporator and condenser sections can be determined by introducing an averaged heat transfer coefficient as

$$\overline{R}_{\text{e}} = \frac{1}{\overline{h}_{\text{eff,e}} A_{\text{e}}} = \frac{L_{\text{e}}}{A_{\text{e}} \int_0^{L_{\text{e}}} h_{\text{eff,e}}(x)\,\mathrm{d}x}, \tag{19}$$

$$\overline{R}_{\text{c}} = \frac{1}{\overline{h}_{\text{eff,c}} A_{\text{c}}} = \frac{L_{\text{eff,c}}}{A_{\text{c}} \int_{L_{\text{e}}+L_{\text{a}}}^{L_{\text{e}}+L_{\text{a}}+L_{\text{eff,c}}} h_{\text{eff,c}}(x)\,\mathrm{d}x}, \tag{20}$$

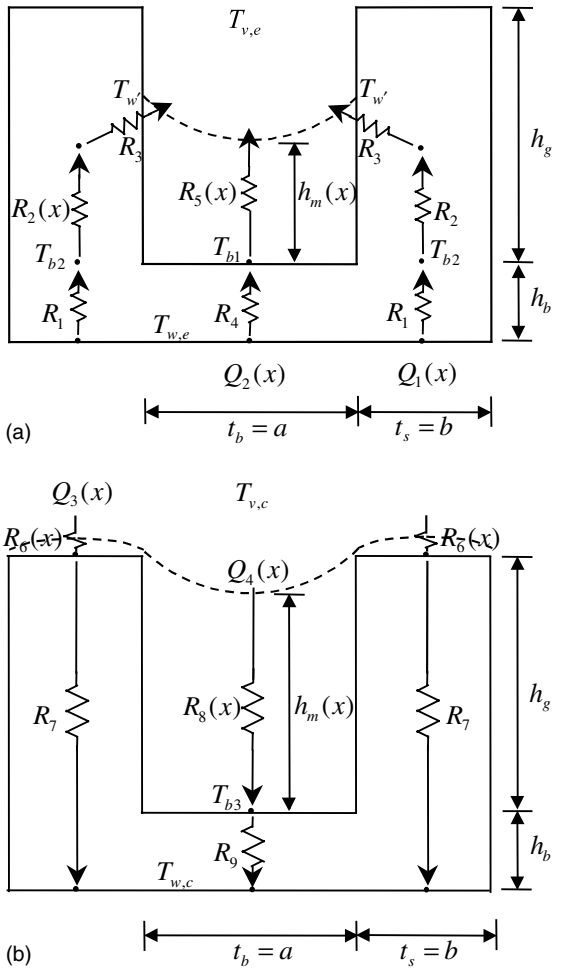

Fig. 2. Heat flow paths and the thermal resistances: (a) evaporator section and (b) condenser section.

where

$$A_{\text{e}} = N(t_{\text{s}} + t_{\text{b}})L_{\text{e}}, \quad A_{\text{c}} = N(t_{\text{s}} + t_{\text{b}})L_{\text{eff,c}}.$$

For the heat flow in the evaporator section, Chi [13] assumed that heat travels through two parallel paths: one is through the groove fin and then through a microfilm region formed at the liquid–fin interface, $Q_1(x)$ in Fig. 2(a) and the other is directly through the liquid in the groove, $Q_2(x)$ in Fig. 2(a). In that case, the heat flux and the local heat transfer coefficient at the evaporator section reduce to

$$q_{\text{in}} = \frac{Q_{\text{in}}}{L_{\text{e}}} = N[Q_1(x) + Q_2(x)] = h_{\text{eff,e}}(x)N(t_{\text{s}} + t_{\text{b}})(T_{\text{w,e}} - T_{\text{v,e}}), \tag{21}$$

$$h_{\mathrm{eff,e}}(x)(t_s+t_b)=\frac{1}{R_e(x)}=\frac{R_1+R_2(x)+R_3+R_4+R_5(x)}{\{R_1+R_2(x)+R_3\}\{R_4+R_5(x)\}}, \quad (22)$$

where

$$R_1=\frac{h_b}{k_s b}, \quad R_2(x)=\frac{h_m(x)}{k_s b}, \quad R_3=\frac{1}{\bar{h}h_g},$$
$$R_4=\frac{h_b}{k_s a}, \quad R_5(x)=\frac{h_m(x)}{k_l a}.$$

The evaporation heat transfer in a groove is mainly due to evaporation in the microfilm region. Chi [13] accounted for this thin film evaporation by introducing the film heat transfer coefficient, $\bar{h}$, as

$$\bar{h}=k_l/(0.185b). \quad (23)$$

In the condenser section, on the other hand, the vapor is assumed to condense over the entire surface as shown in Fig. 2(b). In this case, heat is conducted through two separate paths: one is through the thin liquid film on top of the fin and the through the fin, and the other is through the liquid in the groove. The heat flux and the local heat transfer coefficient in the condenser section can be formulated as

$$q_{in}=\frac{Q_{in}}{L_{\mathrm{eff,c}}}=N[Q_3(x)+Q_4(x)]=h_{\mathrm{eff,c}}(x)N(t_s+t_b)(T_{w,c}-T_{v,c}), \quad (24)$$

$$h_{\mathrm{eff,c}}(x)(t_s+t_b)=\frac{1}{R_c(x)}=\frac{R_6(x)+R_7+R_8(x)+R_9}{\{R_6(x)+R_7\}\{R_8(x)+R_9\}}, \quad (25)$$

where

$$R_6(x)=\frac{\bar{\delta}(x)}{k_l b}, \quad R_7=\frac{(h_g+h_b)}{k_s b},$$
$$R_8(x)=\frac{h_m(x)}{k_l a}, \quad R_9=\frac{h_b}{k_l a}.$$

In the present study, the averaged condensate film thickness $\bar{\delta}(x)$ is evaluated from the heat transfer model at the condenser section suggested by Khrustalev and Faghri [4].

Using Eqs. (22), (23), and (25), numerical integration in Eqs. (19) and (20) can be performed to produce the averaged thermal resistance of each section based on the information about $h_m(x)$ which can obtained from the results of Section 2.1.

3. Experimental investigation

In order to verify the proposed mathematical model, experiments for measuring the maximum heat transport rate and the thermal resistance are conducted and the experimental data are compared with the numerical results obtained from the model. An experimental apparatus for the heat pipe performance test is composed of the evaporator section, the adiabatic section, and the condenser section as shown in Fig. 3. Dots in Fig. 3 denote locations for temperature measurement.

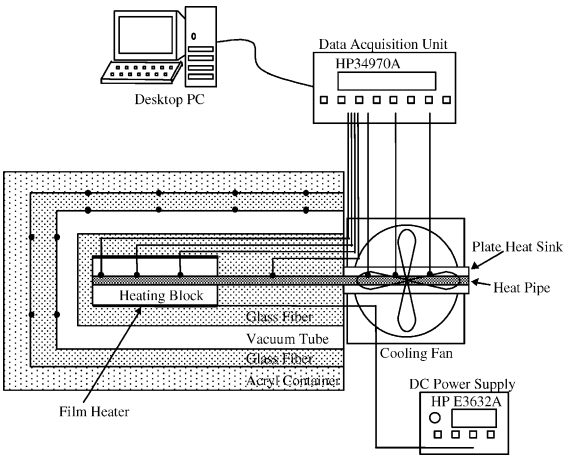

Fig. 3. Schematic diagram of the experimental apparatus.

At the evaporator section, a thin film heater provides uniform heat flux to the upper and lower heating blocks attached to the heat pipe. Three thermocouples are soldered onto the outer wall of the evaporator section, rolled around the heat pipe and pass through the holes through the upper heating block. In order to reduce the contact resistance, thermal grease (OMEGATHERM 201) is applied at all the contacting surfaces of the heat pipe. A plate heat sink is mounted at the condenser section. Three thermocouples are also instrumented on the outer wall of the condenser section as in the evaporator section. Although two thermocouples were installed on the adiabatic section ($x=0.13$ and 0.17 m) in the early stage of the experiments, the temperature difference between the two locations was found to be so small that the adiabatic section could be assumed to be an almost isothermal region. Therefore, one thermocouple is attached to the center of the adiabatic section ($x=0.15$ m) and the working temperature is regarded as the temperature at that point.

All the thermocouples are K-type (36Gage, 0.0127 mm in wire diameter, produced by OMEGA Engineering, Inc.) and rolled circumferentially around the wall to minimize conduction heat losses through the thermocouple wires. The film heater is a standard Kepton thermofoil heater (MINCO Products) with a resistance of $23.3\Omega\pm10\%$. It is powered by a DC power supply with an accuracy of $\pm0.023\%$ to the full-scale range, which is manufactured by Agilent Technologies. Temperature distributions of the heat pipe and the insulation layer were observed and recorded by HP34970A, a data

acquisition unit with an accuracy of 1.0 °C manufactured by Agilent Technologies.

The evaporator section and adiabatic sections are insulated by ceramic fiber, the thermal conductivity of which is 0.055W/mK, and a vacuum tube in order to reduce the heat loss from the experimental apparatus. Although there are insulation layers enclosing the evaporator and the adiabatic sections, the associated heat loss increases as the working temperature of the heat pipe increases. To account for this heat loss, temperatures are measured at 16 points on the ceramic fiber insulation layer that covers the vacuum tube with K-type thermocouples (30Gage, 0.0254 mm in wire diameter, produced by OMEGA Engineering) as shown in Fig. 3. The total heat loss from the apparatus is calculated using a one-dimensional conduction equation.

The maximum heat transport rate is regarded as the maximum heat input rate minus the total heat loss that does not cause partial dry-out at the beginning of the evaporator section at the specified working temperature. The experimental procedure can be summarized as follows:

(1) Warm up the heat pipe by supplying the power to the film heater until the temperature at the adiabatic section reaches a specified working temperature.
(2) Once the working temperature is obtained, increase the heat load and adjust the speed of the cooling fan carefully to maintain the working temperature.
(3) Repeat step (2) until dry-out at the beginning of the evaporator section is observed, which can be detected by a sudden temperature rise in the evaporator section.
(4) Record all the temperatures of the experimental apparatus and the heat input rate. Calculate the maximum heat transfer rate and the overall thermal resistance.

The working temperatures are chosen to be 40, 50, 60, and 70 °C, which are in a typical temperature range for electronic equipment cooling applications of heat pipes. Two samples of each a 3 and 4 mm heat pipe, for a total of four heat pipes, are tested. To verify the reliability of the experimental results, the experimental procedure for each heat pipe is repeated three times per the specified working temperature. All experimental results are averaged values of six experimental results from two heat pipes with the same outer diameter at the specified working temperature.

Geometric parameters of the grooved wick structure and other relevant specifications of the experiment are summarized in Table 2. In order to measure the precise values of the geometric variables, Scanning Electron Microscope (SEM) pictures are used. Also, the initial liquid charge rate is measured by a high precision-weighing machine with an accuracy of 10^{-4} g.

Table 2
Specifications of the heat pipe with the grooved wick structure

	OD 3 mm	OD 4 mm
Number of groove (N) (ea.)	26	40
Vapor core radius (R_v) (mm)	1.091	1.588
Groove depth (h_g) (mm)	0.131	0.141
Groove bottom width (t_b) (mm)	0.123	0.0915
Groove wall inclination angle (ζ) (°)	84	76
Working fluid	Water	
Initial amount of liquid charge (g)	0.15	0.20
Solid material	Copper	
Solid/liquid contact angle (°) [14]	33	
Evaporator section length (cm)	10	
Adiabatic section length (cm)	10	
Condenser section length (cm)	9.5	
Inclination of heat pipe (°)	0	
Working temperature (°C)	40, 50, 60, 70	
Manufacturer	Furukawa Electric	

4. Results and discussion

In Fig. 4(a), the numerical results are compared with the experimental data for the maximum heat transport rate of OD 3 and 4 mm heat pipes with a grooved wick structure. For experimental data reduction, we consider both the bias error from the thermocouples and the precision error from the repeatability of the experimental data. The uncertainty evaluation is performed in accordance with a 95% confidence interval. Also, the amount of heat loss with respect to heat input rate for OD 3 and 4 mm heat pipes is about 28–32% and 15–21% for the temperature range tested. When the experimental data for the maximum heat transport rate are compared with the numerical results, the maximum error is 3.8%. The close agreement between the numerical results and experiment data demonstrates the appropriateness of the proposed model in the working temperature range of 40–70 °C.

Also, we can manifest the importance of the models for the Poiseuille number and the correction factor α in Fig. 4(b). Hufschmidt et al. [11] derived the analytic solutions for the Poiseuille number and α in an open rectangular channel with counter and co-current vapor flow at the flat liquid–vapor interface. However, their solution is restricted to a rectangular channel, and does not account for the effect of the meniscus curvature and the contact angle. If we use their solution to calculate the Poiseuille number and α instead of the present model, the maximum error is 99% compared with experimental data as shown in Fig. 4(b).

Fig. 5(a) shows the liquid and vapor pressure distributions along the axial length of the heat pipe obtained from the mathematical model. Note that the vapor pressure gradient equation (12), takes three different forms; one equation for each section, to account for mass transfer phenomena at the evaporator section and

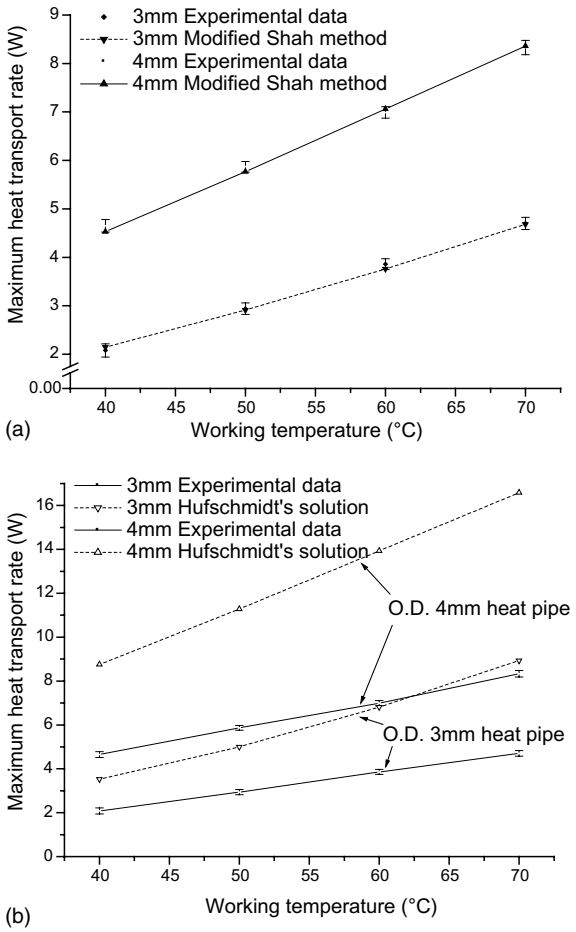

Fig. 4. Results for the maximum heat transport rate: (a) comparison of the numrical results with the experimental data and (b) comparisons of the results using the Hufschmidt's solution with experimental data.

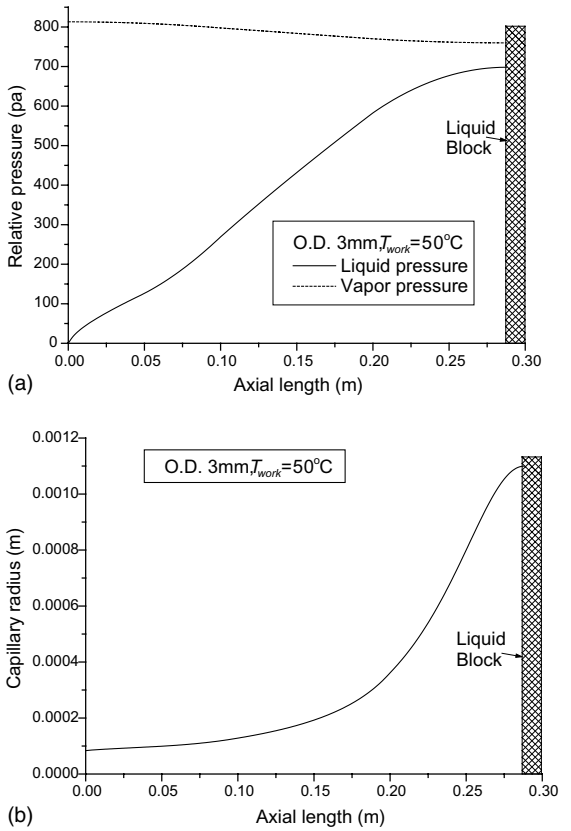

Fig. 5. Liquid and vapor pressure and capillary radius distributions along the axial length of the heat pipe obtained from the mathematical model: (a) liquid and vapor pressure distributions and (b) capillary radius distribution.

condenser sections. These mass transfer phenomena influence the velocity and pressure distributions along the vapor core: the evaporated particles accelerate the vapor flow and cause an additional pressure drop, while condensing particles decelerate the vapor flow and cause a pressure recovery. However, there is no mass transfer in the radial direction in the adiabatic section, and the vapor flow in the adiabatic section becomes a Hagen–Poiseuille flow. A close look at the vapor pressure distribution in Fig. 5(a) reveals these phenomena well.

Fig. 5(b) shows that the capillary radius increases non-linearly along the axial direction and begins to increase rapidly at the beginning of the condenser section. This implies that the difference in the pressure gradient between the liquid and the vapor begins to decrease rapidly at the condenser section because the capillary radius is inversely proportional to the pressure difference between the liquid and the vapor.

Table 3 compares the experimental data with the numerical results for the thermal resistance of the miniature heat pipe between the evaporator and condenser sections at the specified working temperature. The maximum error in the total thermal resistance of OD 3 and 4 mm heat pipes based on the proposed model is within 12.0% and 16.2%.

In order to enhance the thermal performance of the heat pipe under consideration, an optimization of the wick structure for the maximum heat transport rate and the thermal resistance is performed. If we reduce t_b without changing ζ and the number of grooves in Fig. 1(b), t_s will be increased and the groove will eventually be formed in a narrower fashion. This leads to higher capillary pumping force. At the same time, however, the reduction of t_b causes the reduction of A_p, which results in higher flow resistance. This counteraction finally contributes to either an increase or a decrease in the performance of the heat pipe. Also, changes in the groove design influence the total thermal resistance of

Table 3
Comparison of the numerical results with the experimental data for the thermal resistance

OD 3 mm heat pipe			
T_{work} (°C)	40	50	60
$\overline{R}_e$ (°C/W)	0.069	0.068	0.068
$\overline{R}_a$ (°C/W)	0.064	0.021	0.012
$\overline{R}_c$ (°C/W)	0.0079	0.0083	0.0084
$\overline{R}_{tot}$ (°C/W)	0.14	0.097	0.088
ΔT_{exp} (°C)	0.33	0.31	0.37
$\overline{R}_{tot,exp}$ (°C/W)	0.15	0.11	0.10
OD 4 mm heat pipe			
T_{work} (°C)	40	50	60
$\overline{R}_e$ (°C/W)	0.039	0.039	0.039
$\overline{R}_a$ (°C/W)	0.014	0.0055	0.0024
$\overline{R}_c$ (°C/W)	0.0076	0.0077	0.0077
$\overline{R}_{tot}$ (°C/W)	0.061	0.052	0.049
ΔT_{exp} (°C)	0.30	0.29	0.31
$\overline{R}_{tot,exp}$ (°C/W)	0.066	0.049	0.043

the heat pipe. Since the heat pipes in the present study are commercial ones and have fixed grooved wick designs, a parametric experimental study on the effect of various t_b is impossible. However, it is regarded that the proposed model is valid for optimizing Q_{max} and $\overline{R}_{tot}$ with different values of t_b.

The effects of the optimization parameter t_b on the heat pipe performance are evaluated numerically and shown in Fig. 6. From the result of the thermal optimization, a narrow and deep groove has higher heat transport capability and higher overall thermal resistance. The maximum heat transport rate of an OD 3 and 4 mm heat pipe with an optimized groove wick structure can be enhanced up to 48% and 73% and the total thermal resistance can be reduced up to 7% and 11% from the existing configurations.

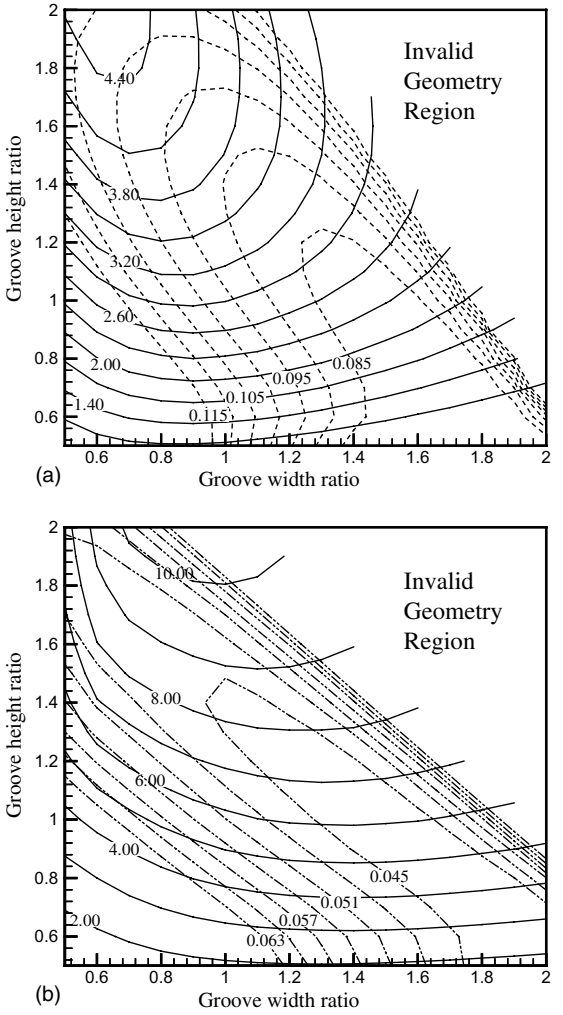

Fig. 6. Thermal optimization of OD 3 and 4 mm heat pipes ($T_{work} = 50$ °C) ((solid line) maximum heat transport rate and (dashed line) overall thermal resistance): (a) OD 3 mm heat pipe and (b) OD 4 mm heat pipe.

5. Conclusion

A one-dimensional mathematical model for a miniature heat pipe with a grooved wick structure has been developed to predict the thermal performance characteristics including the effects of shear stress at the liquid–vapor interface, the initial liquid charge, and the contact angle. In particular, a novel method called a modified Shah method is suggested and validated; this method is an essential feature of the proposed model and accounts for the effect of the liquid–vapor interfacial shear stress. The analytical results based on the modified Shah method are compared with those of previous investigations and excellent agreement is achieved. In order to verify the proposed model, experiments for measuring the maximum heat transport rate and the thermal resistance are conducted. The analytical results for the maximum heat transport rate and the total thermal resistance based on the proposed model are shown to be in relatively good agreement. From the numerical model, we obtain the capillary radius distribution, as well as the liquid and vapor pressure distributions along the heat pipe under steady-state operation. Also, the model is used for the thermal optimization of the grooved wick structure with respect to the width and the groove height. As a result, the maximum heat transport rate of OD 3 and 4 mm heat pipes with an optimized groove wick structure can be enhanced up to 48% and 73%, respectively and the total thermal resistance can be reduced up to 7% and 11%, respectively, from the existing configurations.

Acknowledgements

This work was supported by ETRI (Electronics and Telecommunications Research Institute) and KISTEP (Korea Institute of Science & Technology Evaluation and Planning) under grant number 2-578 through the National Research Lab Program.

Appendix A. Mathematical formulation and verification of the modified Shah method

For simple flow passages with a circular or rectangular cross-section, the velocity field and pressure distributions can be derived using an analytic method. However, it is difficult to obtain the flow characteristics analytically for an open channel with an arbitrary cross section, which in turn requires heavy reliance on extensive CFD simulations or expensive experiments. In order to eliminate this difficulty, a new method based on the one proposed by Shah [15] is suggested to determine the flow characteristics for an open channel with an arbitrary cross section where counter-current flow exists across the open interface.

The governing equation and boundary conditions for fully-developed liquid flow along an open channel with an arbitrary and constant cross section, and counter-current flow at the open interface (shown in Fig. 7) can be expressed by

$$\nabla^2 u_l = \frac{1}{r}\frac{\partial}{\partial r}\left(r\frac{\partial u_l}{\partial r}\right) + \frac{1}{r^2}\frac{\partial^2 u_l}{\partial \theta} = \frac{1}{\mu_l}\frac{dP_l}{dz} = C_1, \tag{A.1}$$

BCs

$$u_l = 0 \quad \text{on } \Gamma_{wall}$$
$$\tau_l = -\tau_v \quad \text{on } \Gamma_{interface}$$

By applying the following transformation in Eq. (A.2), as Shah [15] suggested, the governing equation and the boundary condition can be reduced to Eq. (A.3)

$$-\frac{u_l}{C_1} = u_l^* - \frac{r^2}{4}, \tag{A.2}$$

$$\nabla^2 u_l^* = 0, \tag{A.3}$$

BCs

$$u_l^* = \frac{r_i^2}{4} \quad \text{on } \Gamma_{wall}$$
$$\mu_l\left(\frac{\partial u_l}{\partial n}\right) = -\mu_v\left(\frac{\partial u_v}{\partial n}\right) \quad \text{on } \Gamma_{interface}$$

where n represents the normal direction to the liquid–vapor interface. Assuming that the vapor velocity at the interface equals zero, the liquid velocity gradient term in the above boundary condition becomes

$$\left(\frac{\partial u_l}{\partial n}\right) = -\frac{\mu_v}{\mu_l}\left(\frac{\partial u_v}{\partial n}\right) = \frac{fRe_{h,v}}{2D_{h,v}}\frac{\mu_v}{\mu_l}\bar{u}_v. \tag{A.4}$$

In the meantime, Eq. (A.3) has a series solution in the form of

$$u_l^* = a_0 + \sum_{j=1}^{N} r^j\left(a_j\cos(j\theta) + b_j\sin(j\theta)\right) \tag{A.5}$$

or

$$-\frac{u_l(r,\theta)}{C_1} = -\frac{r^2}{4} + a_0 + \sum_{j=1}^{N} r^j\left(a_j\cos(j\theta) + b_j\sin(j\theta)\right). \tag{A.6}$$

Differential form of Eq. (A.6) yields

$$\begin{aligned}-\frac{1}{C_1}\frac{\partial u_l(r,\theta)}{\partial n} &= -\frac{r}{2}\left(\frac{\partial r}{\partial n}\right) + \sum_{j=1}^{N} jr^{j-1}\left[\cos(j\theta)\left(\frac{\partial r}{\partial n}\right)\right. \\ &\quad \left. - r\sin(j\theta)\left(\frac{\partial \theta}{\partial n}\right)\right]a_j \\ &\quad + \sum_{j=1}^{N} jr^{j-1}\left[\sin(j\theta)\left(\frac{\partial r}{\partial n}\right) + r\cos(j\theta)\left(\frac{\partial \theta}{\partial n}\right)\right]b_j.\end{aligned} \tag{A.7}$$

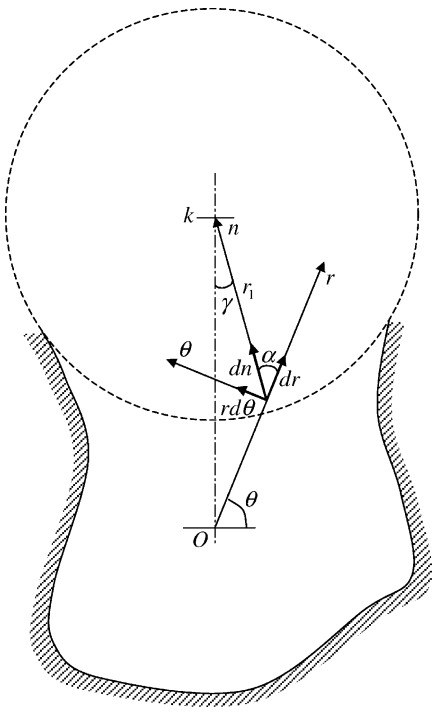

Fig. 7. Schematic view of a channel with an open and arbitrary cross-section.

From Eq. (A.5), u_l^* can be evaluated as long as we determine the $2N+1$ unknown coefficients a_0, a_j, and b_j. This can be done by applying boundary conditions at the wall and the liquid–vapor interface. Along the wall, n points are selected to conform to the geometry of the open channel and a no slip condition is applied to generate n boundary conditions for Eq. (A.6). Similarly, m points are selected along the liquid–vapor interface where the continuous shear stress condition is applied to generate m boundary conditions for Eq. (A.7). Since $n+m=2N+1$, these $2N+1$ equations generated from Eqs. (A.6) and (A.7) can be solved using linear algebra. Also, two gradient terms in Eq. (A.7) can be derived from a geometric relationship by assuming a circular interface as

$$\frac{\mathrm{d}r}{\mathrm{d}n} = \sin\theta\cos\gamma \mp \cos\theta\sin\gamma, \tag{A.8}$$

$$\frac{\mathrm{d}\theta}{\mathrm{d}n} = \frac{1}{r}(\cos\theta\cos\gamma \pm \sin\theta\sin\gamma), \tag{A.9}$$

where

$$\cos\gamma = \frac{k^2+r_1^2-r^2}{2kr_1}, \quad \sin\gamma = \sqrt{1-\left(\frac{k^2+r_1^2-r^2}{2kr_1}\right)^2}.$$

To evaluate the ratio of the actual liquid pressure drop with the counter flow effect included to the ideal liquid pressure drop with no vapor flow effect, as in Eq. (7), iterative calculations are needed and the entire calculation procedure can be summarized as follows (a primed variable denotes that it is affected by non-zero vapor flow).

(1) Generate $2N+1$ equations and solve these equations for, a_0, a_j and b_j in Eqs. (A.4), (A.6), and (A.7) for a no vapor flow case.
(2) Calculate $-\bar{u}_l/C_1$.
(3) Assume the averaged vapor velocity $\bar{u}_v$ and the averaged liquid velocity $\bar{u}_l' = \bar{u}_l$ and take C_1 as C_1'.
(4) Solve the equations for, a_0, a_j and b_j in Eqs. (A.4), (A.6), and (A.7).
(5) Recalculate C_1' based on a_0, a_j and b_j and replace $C_{1,\mathrm{old}}'$ with $C_{1,\mathrm{new}}'$.
(6) Repeat (3) to (5) until $C_{1,\mathrm{old}}' \approx C_{1,\mathrm{new}}'$.
(7) Calculate the pressure drop ratio along the open channel relative to the closed channel with an arbitrary cross-section from following equation.

$$\left(\frac{\mathrm{d}P}{\mathrm{d}z}\right)_1' \Big/ \left(\frac{\mathrm{d}P}{\mathrm{d}z}\right)_1 = \frac{\bar{u}_l'}{\bar{u}_l}\frac{\int_{A_c} f(r,\theta)\,\mathrm{d}A_c}{\int_{A_c} f'(r,\theta)\,\mathrm{d}A_c} = \alpha. \tag{A.10}$$

In order to check the validity of the modified Shah method, numerical results based on modified Shah method are compared with those presented by Ayyaswami et al. [16] and Hufschmidt et al. [11]. In comparison to numerical results by Ayyaswami et al., the maximum error for the Poiseuille number is 0.2% as shown in Fig. 8(a). Also, in comparison to analytic results by Hufschmidt et al., the maximum errors for the Poiseuille number and α are 0.02% and 2%, respectively, as shown in Fig. 8(b). This excellent agreement confirms the validity of the modified Shah method.

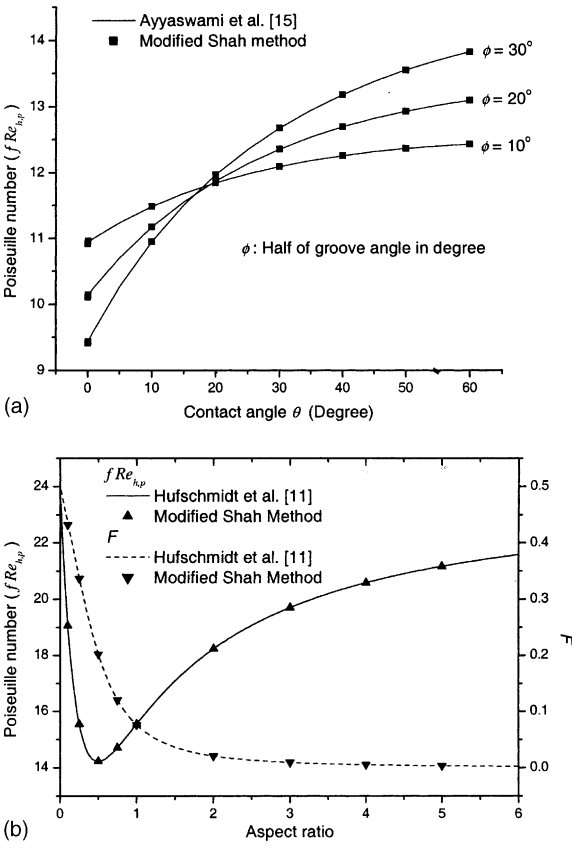

Fig. 8. Verification of the modified Shah method: (a) Comparison of numerical results for Poiseuille number and (b) comparison of results for Poiseuille number and F.

References

[1] T.P. Cotter, Principles and prospects for micro heat pipes, in: Proceedings of the 5th International Heat Pipe Conference, Tsukuba, Japan, 1984, pp. 328–335.
[2] B.R. Babin, G.P. Peterson, D. Wu, Analysis and testing of a micro heat pipe during steady-state operation, in: Proceedings of ASME/AIChE National Heat Transfer Conference, Philadelphia, Pennsylvania, 1989, 89-HT-17.
[3] D. Wu, G.P. Peterson, Investigation of the transient characteristics of a micro heat pipe, J. Thermophys. Heat Transfer 5 (2) (1991) 129–134.
[4] D. Khrustalev, A. Faghri, Thermal analysis of a micro heat pipe, J. Heat Transfer 116 (1994) 189–198.

[5] D. Khrustalev, A. Faghri, Thermal characteristics of conventional and flat miniature axially grooved heat pipes, J. Heat Transfer 117 (1995) 1048–1054.
[6] R. Hopkins, A. Faghri, D. Khrustalev, Flat miniature heat pipes with micro capillary grooves, J. Heat Transfer 121 (1999) 102–109.
[7] N. Zhu, K. Vafai, Analysis of cylindrical heat pipes incorporating the effects of liquid–vapor coupling and non-darcian transport-a closed form solution, Int. J. Heat Mass Transfer 42 (1999) 3405–3418.
[8] M. Oomi, T. Fukumoto, T. Sotani, A heat-pipe system for cooling a desktop computer, Adv. Electron. Packaging 2 (1999) 1951–1955.
[9] B & K Engineering, Summary Report for Axially Grooved Heat Pipe Study, NASA Contract No. NAS5-22562, 1977.
[10] A. Faghri, Heat Pipe Science and Technology, Taylor & Francis, Washington, 1995, pp. 124–125.
[11] E. Hufschmidt, E. Burck, G. Di Cola, H. Hoffman, The Shearing Effect of Vapor Flow on Laminar Liquid Flow in Capillaries of Heat Pipes, NASA TT-F-16601, 1975, pp. 1–21.
[12] A. Faghri, Performance characteristics of a concentric annular heat pipe Part II Vapor flow analysis, J. Heat Transfer 111 (1989) 851–857.
[13] S. Chi, Heat Pipe Theory and Practices: A Sourcebook, Hemisphere Publishing, New York, 1976, pp. 49–51.
[14] V.G. Stepanov, L.D. Volyak, Y.V. Tarlakov, Wetting contact angles for some systems, J. Eng. Phys. 32 (1977) 1000–1003.
[15] R.K. Shah, Laminar flow friction and forced convection heat transfer in ducts of arbitrary geometry, Int. J. Heat Mass Transfer 18 (1975) 849–862.
[16] P.S. Ayyaswami, I. Catton, D.K. Edwards, Capillary flow in triangular grooves, J. Appl. Mech. 41 (1974) 332–336.